

Strain rate dependence of mode II delamination resistance in through thickness reinforced laminated composites

Mehdi Yasaee^{a*}, Galal Mohamed^b, Antonio Pellegrino^c, Nik Petrinic^c, Stephen R. Hallett^b

*a School of Aerospace, Transport and Manufacturing, Building 83, University of Cranfield, Cranfield, MK43 0AL, UK *m.yasaee@cranfield.ac.uk*

b Advanced Composites Centre for Innovation and Science (ACCIS), University of Bristol, Queen's Building, University Walk, Bristol, BS8 1TR, UK

c Department of Engineering Science, Engineering and Technology Building, Parks Road, Oxford OX1 3PJ

Abstract

A thorough experimental procedure is presented in which the mode II delamination resistance of a laminated fibre reinforced plastic (FRP) composite with and without Z-pins is characterised when subjected to increasing strain rates. Standard three-point End Notched Flexure (3ENF) specimens were subjected to increasing displacement loading rates from quasi-static (~0m/s) to high velocity impact (5m/s) using a range of test equipment including drop weight impact tower and a Modified Hopkinson Bar apparatus for dynamic three-point bending tests.

The procedure outlined uses compliance based approach to calculate the fracture toughness which was shown to produce acceptable values of G_{IIC} for all loading rates. Using detailed high resolution imaging relationships between delamination velocities, apparent fracture toughness, longitudinal and shear strain rates were measured and compared. Confirming behaviours observed in literature, the thermosetting brittle epoxy composite showed minor increase in G_{IIC} with increase in strain rate. However, the Z-pinned specimens showed a significant increase in the apparent G_{IIC} with loading rate. This highlights the need to consider the strain rate dependency of the Z-pinned laminates when designing Z-pinned structures undergoing impact.

Keywords

Composites; delamination; impact; fracture toughness; Z-pin

30 **1 Introduction**

31 Environmental, financial and performance requirements in global transport and
32 energy industries necessitates ever more fuel efficient and high performance
33 engineering structures and components. One method to tackle all of these
34 requirements is to reduce the weight of components whilst maintain the same
35 structural performance. For this reason laminated composite materials have seen an
36 increased usage across all these sectors. These materials provide exceptional specific
37 stiffness relative to their metal counter parts, amongst many other benefits such as
38 corrosive resistance and fatigue performance.

39 However, the use of laminated composites does possess some drawbacks. The
40 anisotropy of the material and manufacturing challenges results in a costly product
41 development cycle. Furthermore, laminated composites do not possess any through
42 thickness reinforcements, hence a major failure mechanisms of these materials is de-
43 bonding or delamination of individual ply layers. Although, composite components
44 are by design, capable of carrying in-service stresses, localised out of plane loading in
45 form of impact may generate delamination damage, which will significantly reduce
46 the residual strength of the component.

47 To overcome this limitation it is possible to adopt many ‘damage tolerant design’
48 techniques. Thicker and thus stiffer components will make them more resilient to out
49 of plane loading but with a weight penalty. Use of tougher matrix constituents with a
50 plastic phase will improve the overall performance but only up to a limit [1,2]. Use of
51 interleaving materials at the critical interfaces where delaminations may initiate is
52 another popular method [3,4]. Modern composite systems are increasingly employing
53 such technologies, which have provided significant performance enhancements
54 compared to earlier generations of composite materials.

55 For largescale delamination damage, through thickness reinforcement (TTR)
56 technologies have been shown to be quite effective [5]. In these methods, fibres or
57 small rods are inserted in the composite materials reinforcing the thickness direction
58 of the laminate. One of these techniques, also known as Z-pinning is a popular
59 method used to reinforce pre-preg composite laminates. By inserting small stiff,
60 fibrous composite rods in the thickness direction, this helps bridge the delamination
61 interface tractions and thus provides excellent damage resistance capability [6].

62 Resistance of TTR composites to delamination has been subject to many studies,
63 including quasi-static [6–8] and fatigue loading [9]. However, experimental
64 investigations on the response of TTR composites when subjected to dynamic loading
65 is limited and not well understood.

66 Investigations on the strain rate dependency of the constitutive mechanical properties
67 of composite materials has produced many contradicting results as highlighted by
68 Gerlach *et. al.* [10]. Investigations have shown tensile strength and stiffness can either
69 increase, decrease or be independent of strain rate. Strain rate dependency of
70 delamination fracture toughness has also exposed conflicting results as reviewed
71 comprehensively by Jacob *et. al.* [11], highlighting experimental investigations that
72 have demonstrated increases, decreases and independence of fracture toughness with
73 strain rates. However from a closer look at the literature, some trends becomes
74 apparent. For thermosetting un-toughened epoxy composites, delamination fracture
75 toughness has either an increase [12–14] or no significance [15,16] with increased
76 loading rate. Whereas thermoplastic composites have shown strong negative strain
77 rate dependency, with delamination fracture toughness decreasing with increase in
78 loading rate [15,17–19]. Ductile thermoplastics materials are well known to exhibit

79 brittle fracture when subjected to increased strain rates [20], whereas fracture in brittle
80 epoxies do not exhibit as strong strain rate dependence [21].

81 Dynamic fracture of materials is a specialist field of interest in material engineering
82 [22] with a wide range of studies exploring fracture of materials from the fundamental
83 atomic scale to large geological cases. Of particular interest is the concept of a
84 limiting speed of crack propagation rate ($a' = \partial a / \partial t$) which has been shown to be
85 equal to the materials' shear wave speed (C_s) when loaded in mode I, whilst in mode
86 II the delamination rate can increase beyond the shear wave speed reaching a critical
87 velocity (V_C) which is approximately equal to $\sqrt{2}C_s$ [23]. These extreme shear crack
88 velocities have been achieved in edge notched composite plates where loading is
89 directly transferred to the generation of the crack front, through a specific 1point bend
90 configuration. Measuring crack velocities is challenging and often requires special
91 detection gauges [24] or high resolution, high speed photography in excess of 50,000
92 frames per second (fps) to deduce the crack tip propagation reliably. For this reason
93 only a few investigations exist in literature where delamination velocity in a standard
94 fracture test has been measured. In mode I using a double cantilever beam (DCB),
95 delamination speeds have been shown to reach up to 20-80m/s [15] for loading rate of
96 10m/s. In mode II delamination speeds have shown to reach up to 130m/s using an
97 end loaded split (ELS) specimen [25]. Tsai *et. al.* [24] and Guo *et. al.* [26] used a
98 specific quasi-static test setup in which strain energy at the crack tip was built up with
99 the use of interleaved toughening strips in a 3ENF and DCB specimen respectively.

100 This build of strain energy in the sample thus allowed for control of the propagation
101 rate of the delamination. Using this technique delamination speeds of up to 1100m/s
102 in mode II and 330m/s in mode I were reported, respectively.

103 It is quite evident that loading rate will only influence the fracture toughness of a
104 material when the stress waves travelling in the body directly alter the stress states in
105 the plastic zone ahead of a crack tip. For this reason factors such as loading/boundary
106 conditions as well as geometric shape of the component will greatly influence the
107 dynamic response of a component. Therefore direct comparison of the loading, strain
108 and crack propagation cannot be readily made and could be one major reasons behind
109 contradicting results in literature, particularly in regard to epoxy based composite
110 delaminations.

111 A feature unique to laminated composites that has shown to have a direct dependence
112 on strain rate is the apparent mode II fracture toughness of interlaminar toughening
113 techniques such as interleaving or TTR. Jiang et. al. [27] showed a direct linear
114 increase in fracture toughness of a thermosetting composite with a toughened epoxy
115 interleave phase. With a modest loading rate increase of 1-100mm/min up to 84%
116 increase in apparent G_{IIC} was reported. Colin de Verdiere et. al. [25] reported a
117 modest increase of approximately 26% in the initiation apparent G_{IIC} of tufted
118 composite specimens loaded up to a rate 7m/s. For Z-pinned composites the mode I
119 apparent fracture toughness appears to reduce with an increase in loading rate as
120 shown by Liu et. al. [28].

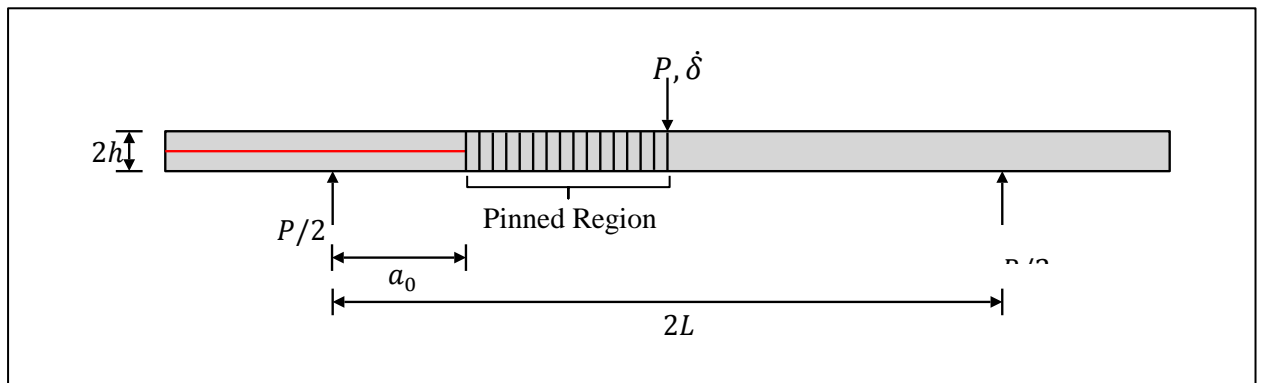
121 There are very few papers in the open literature concerned with the strain rate
122 dependency of Z-pinned composites (e.g. [29]). The objective of this paper was to
123 investigate the mode II aparent fracture toughness of a laminated composite
124 reinforced in the thickness direction using with Z-pins made from carbon fibre
125 reinforced plastic (CFRP) rods. These tests were carried out at displacement loading
126 rates from quasi-static up to 5m/s. A comprehensive analysis of the composite

127 response was made to conclusively show the effect of strain rate on the delamination
128 resistance in un-reinforced and TTR epoxy based composites.

129 **2 Experimental test procedure**

130 **2.1 Materials and specimen preparation**

131 Specimens were manufactured using IM7/8552 prepreg (Hexcel, UK) stacked in a
132 Zero Dominated (ZD) sequence of $[(0, -45, 0, +45)_{3S}]_S$ to achieve a nominal
133 thickness of 6mm, with a 13 μ m PTFE film placed at the mid plane interface to form a
134 starter crack, which falls between two 0 $^\circ$ plies, preventing any out of plane crack
135 migration. The effective laminate properties were calculated using laminate theory
136 and anisotropic material properties of a single UD ply (Table 1) with axis definitions
137 as shown in Figure 2. The test procedure followed the standard 3 point bend end
138 notched flexure (3ENF) [30] shown in Figure 1 with varying loading displacement
139 rates ($\dot{\delta}$).



140
141 **Figure 1 3ENF test setup**

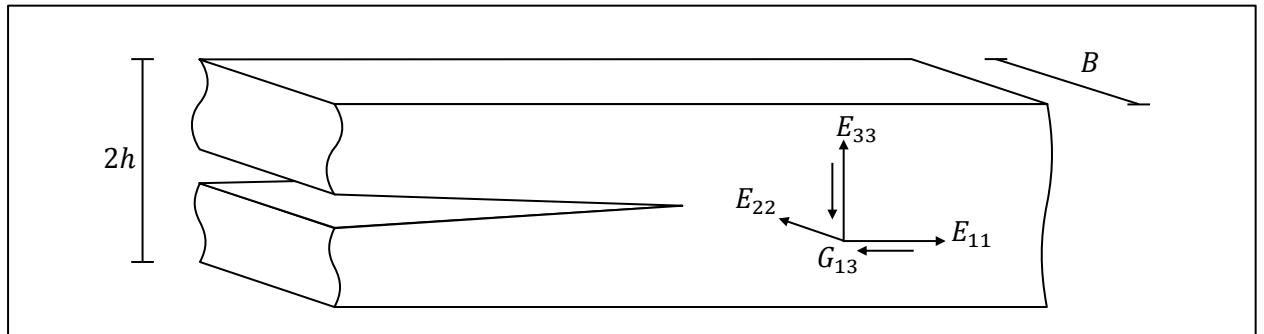
142 The Z-pinned specimens were pinned with T300 carbon/BMI pins arranged in a grid
143 pattern with a spacing of 1.75mm, generating a nominal 2% areal density. Both the
144 control and the Z-pinned samples were machined from a single plate, ensuring
145 consistency in the material properties across both sample sets.

146

Table 1 Effective Properties IM7/8552 laminate in a (0, -45, 0, +45) stacking sequence

E_1	90.83GPa	G_{12}	23.37GPa	ν_{12}	0.71
E_2	26.44GPa	G_{13}	4.86GPa	ν_{13}	0.14
E_3	13.18GPa	G_{23}	4.23GPa	ν_{23}	0.37

147

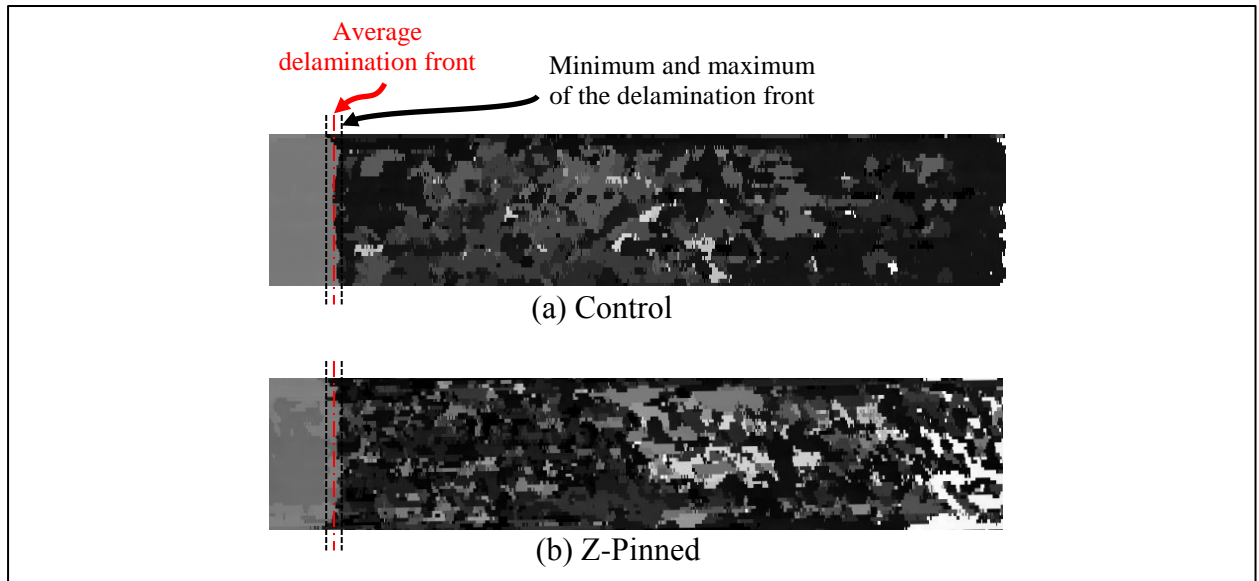


148

149 **Figure 2 Composite laminate axis definitions**150 **2.2 Specimen Preparation**

151 Each specimen was machined to a nominal width of 20mm. The un-cracked part of
 152 each individual specimen was tested in a 3 point bend (3PB) following the ASTM-
 153 790 [31] test standard to measure the flexural modulus (E_{1f}) of the material. The
 154 width (B) and thickness ($2h$) of each specimen was measured at three different
 155 locations along its length to an accuracy of ± 0.05 mm. For each specimen, a natural
 156 mode II pre-crack from the starter film was created using the procedure set out in
 157 ASTM-D7905 [30] to generate an initial crack length (a_0) of 20mm when positioned
 158 in the final test configuration. This resulted in 30mm of uncracked laminate and
 159 reinforced region ahead of the crack for the control and Z-pinned samples
 160 respectively. To ensure that the initial crack length was correctly determined, each
 161 sample was non-destructively tested using an ultrasonic C-scan technique and the
 162 average crack front measured as shown in Figure 3.

163 Each edge of the specimens was painted with a speckle pattern to measure full field
164 strain and obtain accurate displacement measurements.



165
166 **Figure 3** Example of ultrasonic C-scan of (a) control and (b) pinned samples to determine the average
167 natural pre-crack position

168 **2.3 Test procedures**

169 The ENF tests were performed with increasing displacement loading rates from quasi-
170 static (8.3×10^{-6} m/s), to intermediate (1-4 m/s) and high (5.5 m/s) on three different test
171 apparatus. For all tests the support roller half span (L) was set at 50 mm with an initial
172 crack length (a_0) of 20 mm and support roller and loading nose diameter of 10 mm.

173 The displacement and the crack propagation for all tests was monitored using a high
174 definition imaging for quasi-static tests and high speed photography with a minimum
175 of 100,000 fps for the high loading rate tests. The camera was set up to ensure on
176 average a 12 pixel to mm resolution. This ensured sufficient resolution was available
177 for full field strain measurements.

178 **2.4 Quasi-static**

179 The quasi-static 3ENF tests were carried out according to the ASTM-D7905 [30]
180 standard with a loading displacement rates of 0.5 mm/min (8.3×10^{-6} m/s). The load was

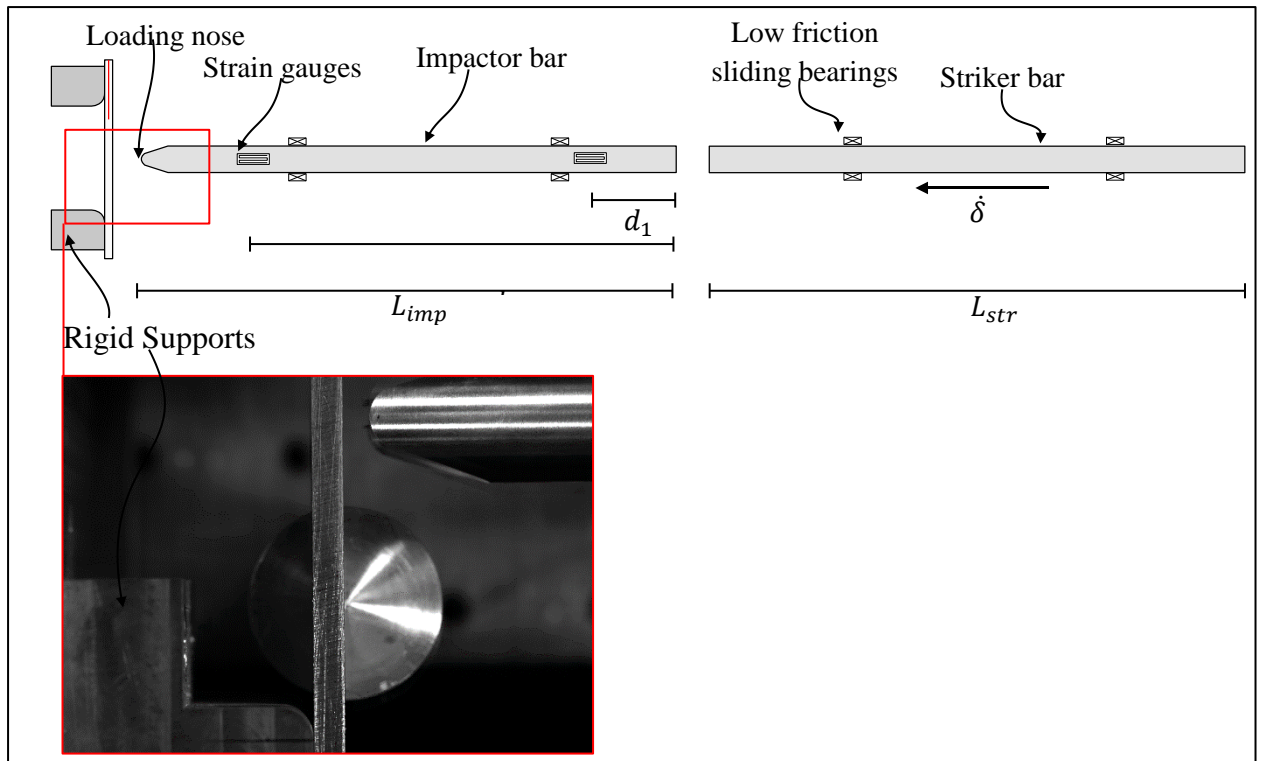
181 measured using a calibrated 5kN load cell on a hydraulic Instron test machine. For
182 these tests, the delamination is unstable for the length of the specimen being
183 measured. Therefore, the maximum load corresponds to the initiation of delamination
184 which is the critical load to use in the data reduction equations.

185 **2.5 Intermediate tests**

186 Intermediate loading displacement rate 3ENF tests were carried out on an
187 instrumented drop weight impact tower. For these tests a cylindrical loading nose was
188 attached to the end of a calibrated piezo-electric load-cell. The loading displacement
189 rate was varied by raising the entire impactor unit weighing 6.21 kg to a specific
190 height above the top surface of the laminate.

191 **2.6 High rate tests**

192 High loading displacement rate 3ENF tests were carried out using a Modified
193 Hopkinson Bar apparatus shown in Figure 4. The setup follows closely the impact
194 bending test procedure carried out by Hallett [32], Gerlach et. al. [33] and Wiegand et.
195 al. [34]. A striker bar of length L_{str} , is accelerated using compressed air to strike an
196 instrumented impactor bar of length L_{imp} with the same mechanical impedance and
197 diameter. This impact then generates a stress pulse of duration of $2L_{str}/c_0$, where
198 $c_0 = \sqrt{E/\rho}$ is the 1D longitudinal wave speed in the bar termed bar velocity. It is
199 desirable to position the first strain gauge at a distance of d_1 such that $L_{str} < (L_{imp} -$
200 $d_1)$ to ensure that the incident pulse and the first reflected pulse from the striker bar
201 does not superimpose. This transfer of kinetic energy then accelerates the impactor
202 bar to a specific impact velocity generating the loading rate required to deform the
203 specimen. The material and geometrical properties for both the striker and the impact
204 bar and the strain gauge positions are given in Table 2.



205

206

Figure 4 SHPB test setup

207

Table 2 SHPB Properties

Material	Titanium Alloy
	Ti-6Al-4V
	(Grade 5)
Modulus, E	113.8GPa
Density, ρ	4430kg/m ³
Striker Bar	
Length, L_{str}	2.7m
Diameter	20mm
Mass	3.758kg
Impactor Bar	
Length, L_{imp}	3.0m

Diameter	20mm
Mass	4.175kg
Strain gauge 1, d_1	0.215m
Strain gauge 2, d_2	1.806m

208

209 Using two strain gauge stations set up in a half-bridge configuration on the impact bar
 210 the magnitude of the stresses at those specific cross section in the bar can be
 211 calculated. The motion of longitudinal waves in a cylindrical bar can be described
 212 using the one-dimensional wave equation:

$$\frac{\partial^2 u}{\partial x^2} = \frac{1}{c_0^2} \frac{\partial^2 u}{\partial t^2} \quad (1)$$

213 The general solution to this wave equation can be expressed in terms of two arbitrary
 214 functions, f and g that define the wave-forms traveling in the positive (forwards) and
 215 negative (backwards) directions respectively.

$$u(x, t) = f(x - c_0 t) + g(x + c_0 t) \quad (2)$$

216 Following standard constitutive relationships, this can be written in the form:

$$\frac{du(x, t)}{dx} = \varepsilon(x, t) = f'(x - c_0 t) + g'(x + c_0 t) = \varepsilon_1(x, t) + \varepsilon_2(x, t) \quad (3)$$

217 Where, $f'(x - c_0 t)$ and $g'(x + c_0 t)$ are replaced by the incident and reflected
 218 strain functions $\varepsilon_1(x, t)$ and $\varepsilon_2(x, t)$ respectively. The stress σ and particle velocity
 219 v at any point in the bar can also be defined using equation (3) as:

$$\sigma(x, t) = E(\varepsilon_1(x, t) + \varepsilon_2(x, t)) \quad (4)$$

$$v(x, t) = -\frac{E}{\rho c_0}(\varepsilon_1(x, t) - \varepsilon_2(x, t)) \quad (5)$$

220 Where ρ is the density, E is the modulus and c_0 is the 1D impactor bar velocity.
 221 Figure 5 shows the Lagrangian (time-distance) diagram for a 1D wave propagation
 222 in a cylindrical bar of length L_{imp} with two strain gauges at a distance d_1 and d_2 from
 223 the striker/impactor contact end ($x = 0$). It is possible to calculate the total stress in
 224 any cross section of the bar including the tip of the impactor using the time shifted
 225 values from the strain gauge instrumentations. In this investigation the location of
 226 interest was at the impactor tip, $x = L_{imp}$. The forward and backward travelling
 227 elastic strain waves at this location was determined using the following routine:

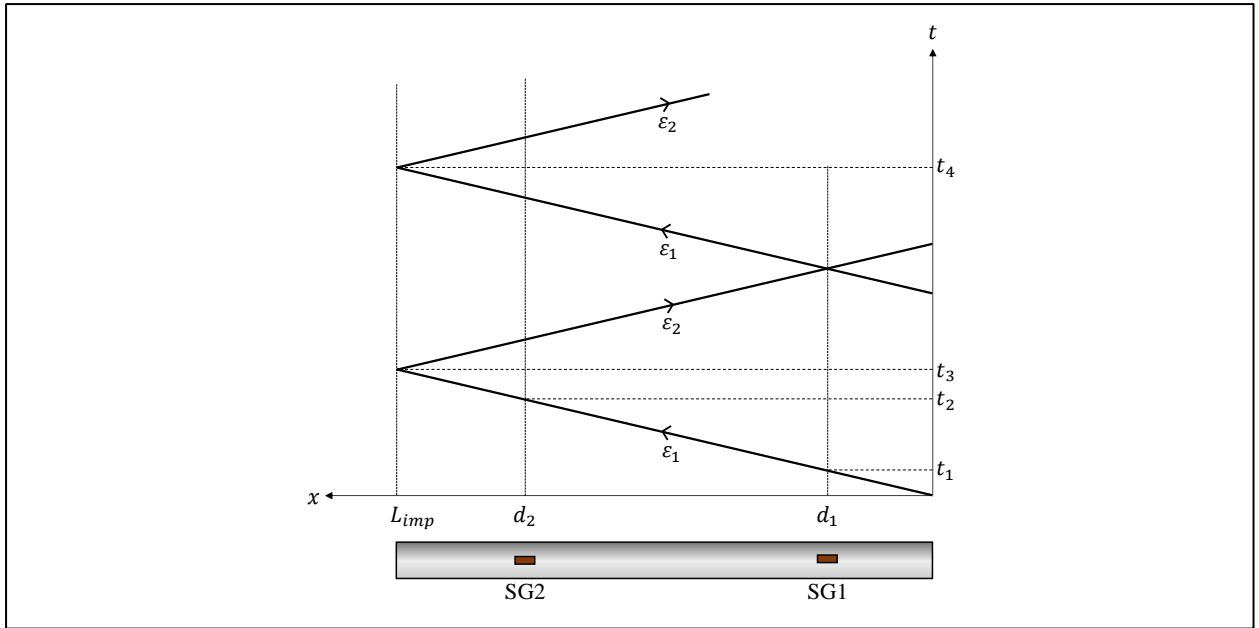
$$\varepsilon_1(L_{imp}, t) = \begin{cases} \varepsilon[d_1, t - (t_3 - t_1)] & t < t_4 \\ \varepsilon[d_1, t - (t_3 - t_1)] - \varepsilon_2[L_{imp}, t - (t_4 - t_1)] & t \geq t_4 \end{cases} \quad (6)$$

$$\varepsilon_2(L, t) \quad (7)$$

$$= \begin{cases} \varepsilon[d_2, t + (t_3 - t_2)] - \varepsilon[d_1, t + (t_3 - t_2) - (t_2 - t_1)] & t < t_4 \\ \varepsilon[d_2, t + (t_3 - t_2)] - \{\varepsilon[d_1, t + (t_3 - t_2) - (t_2 - t_1)] - \varepsilon_2[L_{imp}, t - 2(t_2 - t_1)]\} & t \geq t_4 \end{cases}$$

228 Using equations (6), (7) and (4) the load at the end of an impactor bar with a cross
 229 section area, A is:

$$F(L_{imp}, t) = A\sigma(L_{imp}, t) \quad (8)$$

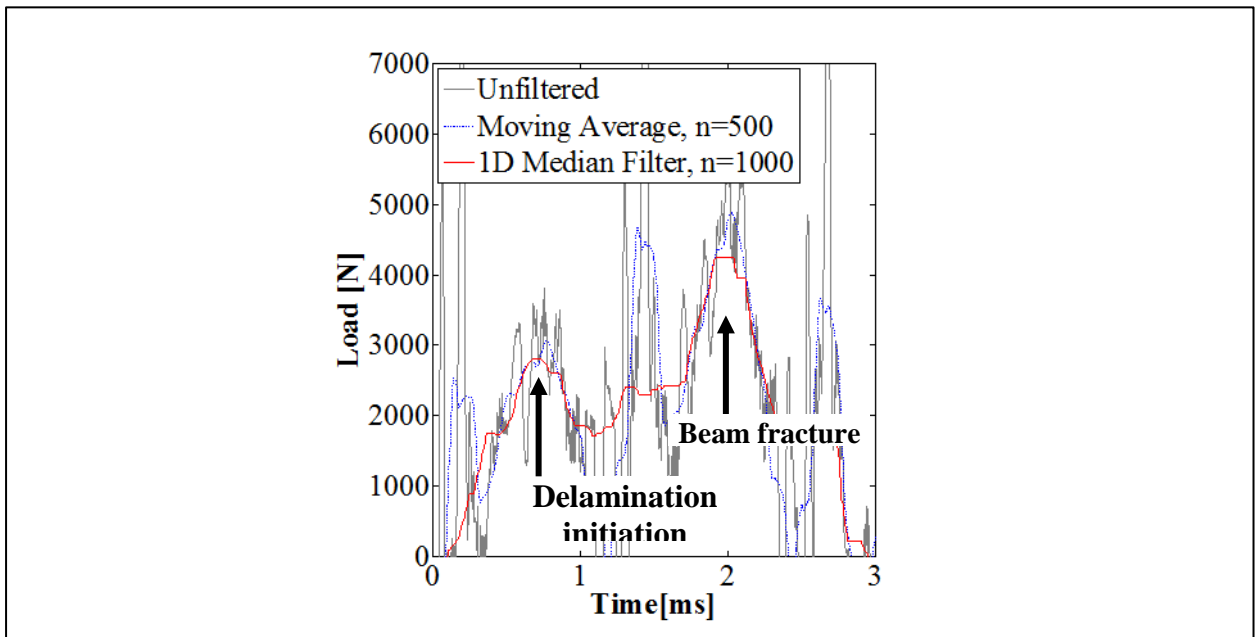


230

231 **Figure 5** Langrangian diagram for longitudinal waves in cylindrical bar

232 The load signal calculated was further filtered to remove high frequency noise. A
 233 1000th order 1D median filter was found to effectively attenuate the high peak signals
 234 which was not possible with a 500 point moving average smoothing technique, Figure
 235 6. This plot also illustrates the load drops associated with delamination initiation and
 236 subsequent fracture, as confirmed by the high speed footage.

237



238

239 **Figure 6** Example of filtration of the calculated load from the SHPB tests

240 The wedge shaped tip of the impactor was designed in order to minimise the effect of
241 stress wave reflections along the impactor rod tip. Gerlach et. al. [33] and Wiegand et.
242 al. [34] have shown using FE analysis that the force obtained from stress wave
243 analysis compares well to the numerical simulations confirming that any inaccuracy
244 introduced by the geometry of the wedged tip is negligible.

245 **2.7 Data reduction technique**

246 Load response of a high rate test procedures suffer from high frequency oscillations
247 arising from dynamic effects as shown in previous section. The load output from the
248 drop-weight impact tower used in these experiments is filtered internally by the test
249 equipment which removes high frequency vibrations however inertial oscillations are
250 still visible in the response. These dynamic effects also increase with increasing
251 loading rates, thereby determining the critical load at the moment of initiation is not
252 possible [15]. For this reason, use of measured critical load in the data reduction
253 calculations will yield incorrect values of the materials fracture toughness.

254 It has been shown that CFRP laminates exhibit no observable strain rate dependency
255 in their axial modulus E_{11} [15,35]. It is thus possible to calculate G_{IIC} using the
256 displacement at the moment of delamination initiation. This displacement can be
257 reliably measured using the high speed photography images from all loading rate test
258 procedures. The compliance of the 3ENF specimen [36] is given by:

$$C = \frac{2L^3 + 3a^3}{8E_{1f}Bh^3} + \frac{3L}{10G_{13}Bh} \quad (9)$$

259 The term on the right includes the influence of through thickness shear which is
260 dependent on the h/L of the test setup. The inter-laminar fracture toughness is
261 calculated by measuring the strain energy release rate of the material, defined as:

$$G = \frac{1}{B} \frac{\partial(W - U)}{\partial a} \quad (10)$$

262 where W is the work applied by external forces and U is the elastic strain energy.

263 Using equation (10) the mode II fracture toughness has been reduced [37] to be:

$$G_{IIC} = \frac{9 \left(\frac{\delta}{C}\right)^2 (a + 0.42\chi h)^2}{16B^2 E_{1f} h^3} \quad (11)$$

$$\chi = \left[\frac{E_{11}}{11G_{13}} \left(3 - 2 \left(\frac{\Gamma}{1 + \Gamma} \right)^2 \right) \right]^{1/2} \quad (12)$$

$$\Gamma = \frac{1.18 \sqrt{E_{11} E_{33}}}{G_{13}} \quad (13)$$

264 Where the term $0.42\chi h$ is the correction added to the length of the crack to account
 265 for the root rotation of the beam arms [37] and E_{1f} is the flexural modulus of the
 266 material which was measured for each specimen independently in the current
 267 experiments. The above equations do include two rate dependent properties, G_{13} and
 268 E_{33} which have been shown to increase by 12% and 25% for strain rates up to $300s^{-1}$
 269 [38]. Assuming a maximum increase of 25% for these two properties will result in a
 270 decrease of 0.11% in the calculated value of G_{IIC} . Therefore, any rate dependency of
 271 G_{13} and E_{33} can be ignored.

272 In the high rate tests it has been argued that the kinetic energy of the body may
 273 influence the strain energy release rate at the crack tip [17]. The total kinetic energy of
 274 the system is defined as:

$$T = \frac{1}{2} \rho_c B (2h) \int_{-L}^L \left(\frac{d\delta}{dt} \right)^2 dx \quad (14)$$

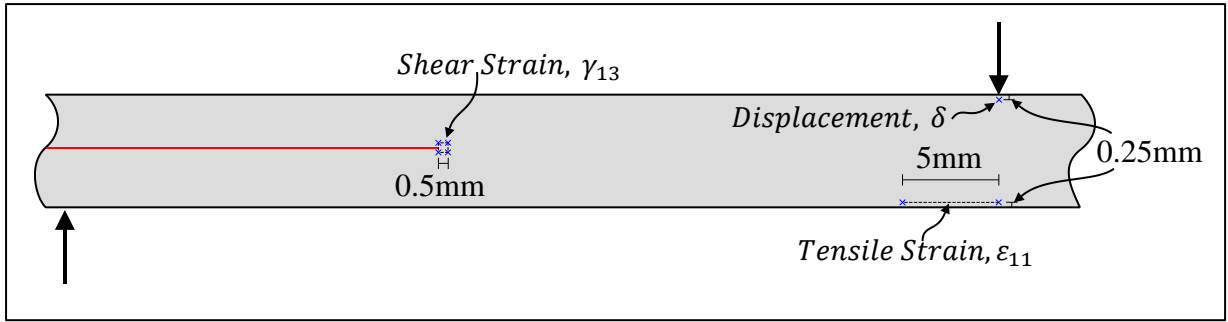
275 Where ρ_c is the density of the specimen being tested. Therefore the kinetic energy
276 contribution to the strain energy release rate, G (equation (10)) for a specimen with
277 $a/L = 0.5$ was defined to be [17]:

$$\frac{1}{B} \frac{\partial T}{\partial a} = -0.078 \rho h \dot{\delta} \quad (15)$$

278 For the experimental loading rates (maximum $\dot{\delta} \approx 5.5m/s$) investigated, the kinetic
279 energy term can be seen to increase the fracture toughness by less than 1% of G_{IIC} .
280 Therefore it can be reasonably assumed that, for the tests carried out in this
281 investigation, the kinetic energy contribution is negligible and the quasi-static G_{IIC}
282 data reduction procedure to be valid.

283 **2.8 Tensile and Shear strain rate measurement**

284 The displacement, shear and tensile strains were measured using images extracted
285 from video frames in quasi static tests and from high speed photography in the high
286 rate tests. These image sequences were then post processed using a non-contact video
287 extensometer software (Imetrum Ltd) to track specific points on the sample as shown
288 in Figure 7. To verify these measurements, full field strain measurements were carried
289 out using 2D digital image correlation (GOM UK Ltd) for a specimen in each test
290 regime using the same image sequences. A least squares polynomial fit of the first
291 degree (linear fit) was applied to the initial elastic region section of the strain curves
292 to determine the strain rates for all samples respectively.



293

294

Figure 7 Displacement, tensile and shear strains measured using non-contact video extensometer

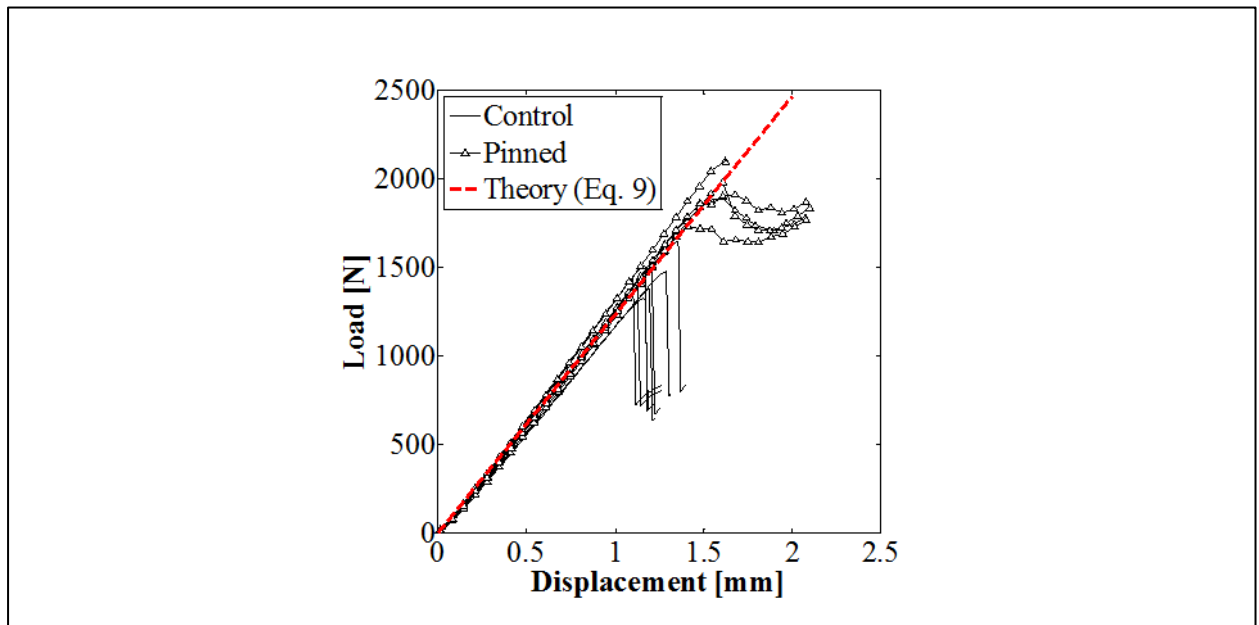
295

296 3 Results

297 3.1 Quasi-Static – Data reduction method comparison

298 The load-displacement plot of the control and pinned samples is shown in Figure 8.

299 The quasi-static flexural tests of all the samples produced an average flexural
300 modulus, E_{1f} of 83.5 ± 1.1 GPa. Figure 8 shows the theoretical compliance, calculated
301 using this flexural modulus with $a = 20$ mm, $B = 20$ mm. The mode II fracture
302 toughness of the initial non pre-crack (from 13 μ m PTFE release film) was measured
303 to be 1050 ± 156 J/m². Following the standard ASTM 3ENF test procedure the fracture
304 toughness of the natural pre-crack G_{IIC} of the IM7/8552 was measured to be
305 663 ± 100 J/m². Calculating the G_{IIC} using the compliance procedure described in
306 section 2.7 and equation (11) the fracture toughness was measured to be
307 673 ± 112 J/m². With only 1.5% difference between the two procedures, the compliance
308 procedure can be accepted to produce correct values of the fracture toughness of the
309 material and gives confidence to use for the high rate procedure.



310

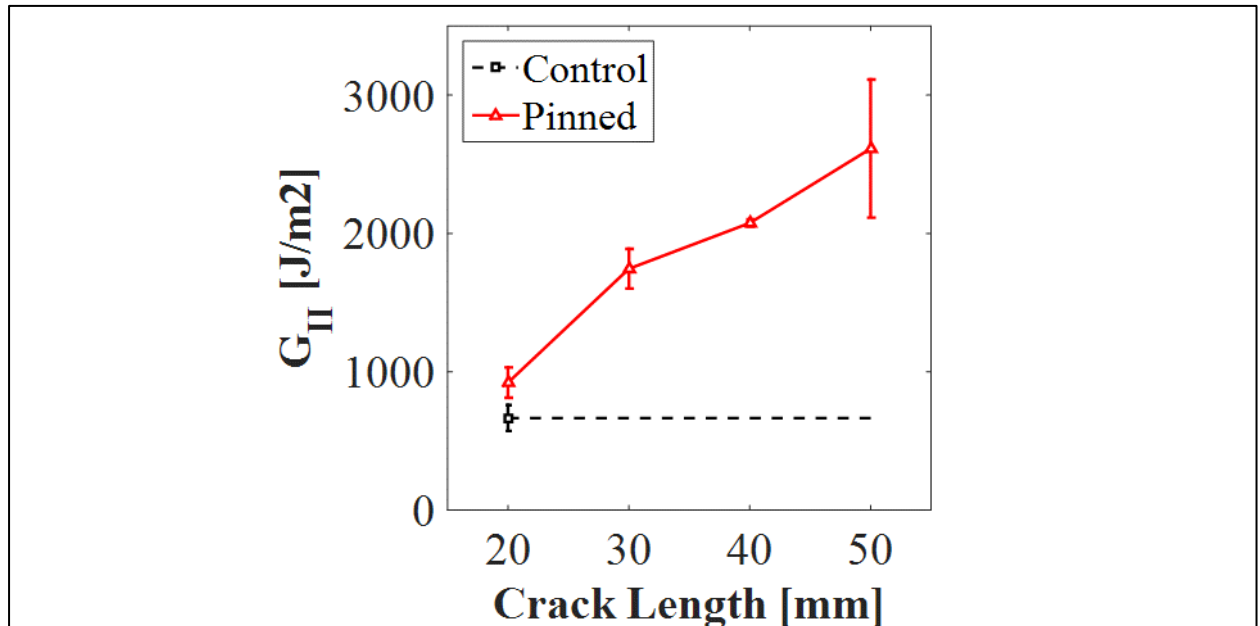
311 Figure 8 Load-displacement for control specimens along with average compliance using equation (9)

312 The average R curve for the control and pinned samples are shown in Figure 9. For

313 control samples, the 3ENF only produces a single critical strain energy release rate

314 value at the moment of initiation due to the unstable nature of the crack, which is the
315 fracture toughness, G_{IIc} of the material. The pinned samples however produce an
316 increasing R curve with crack length due to the development of the extrinsic bridging
317 zone behind the crack tip. The average critical strain energy release rate at the
318 moment of initiation is $922 \pm 109 \text{ J/m}^2$, a minor increase relative to the control samples.
319 The critical strain energy release rate reaches a maximum of $2613 \pm 499 \text{ J/m}^2$ at a crack
320 length of 50mm. In this test configuration the maximum bridging zone length possible
321 is 30mm, however the fully developed Z-pin bridging zone length is expected to be
322 much longer than the 30mm length, approximately between 40-60mm [39]. The
323 apparent fracture toughness increase of these tests agrees well with that previously
324 reported in literature [6,39,40].

325



326

327 Figure 9 Average R curve for control and pinned specimens

328 3.2 Delamination velocity

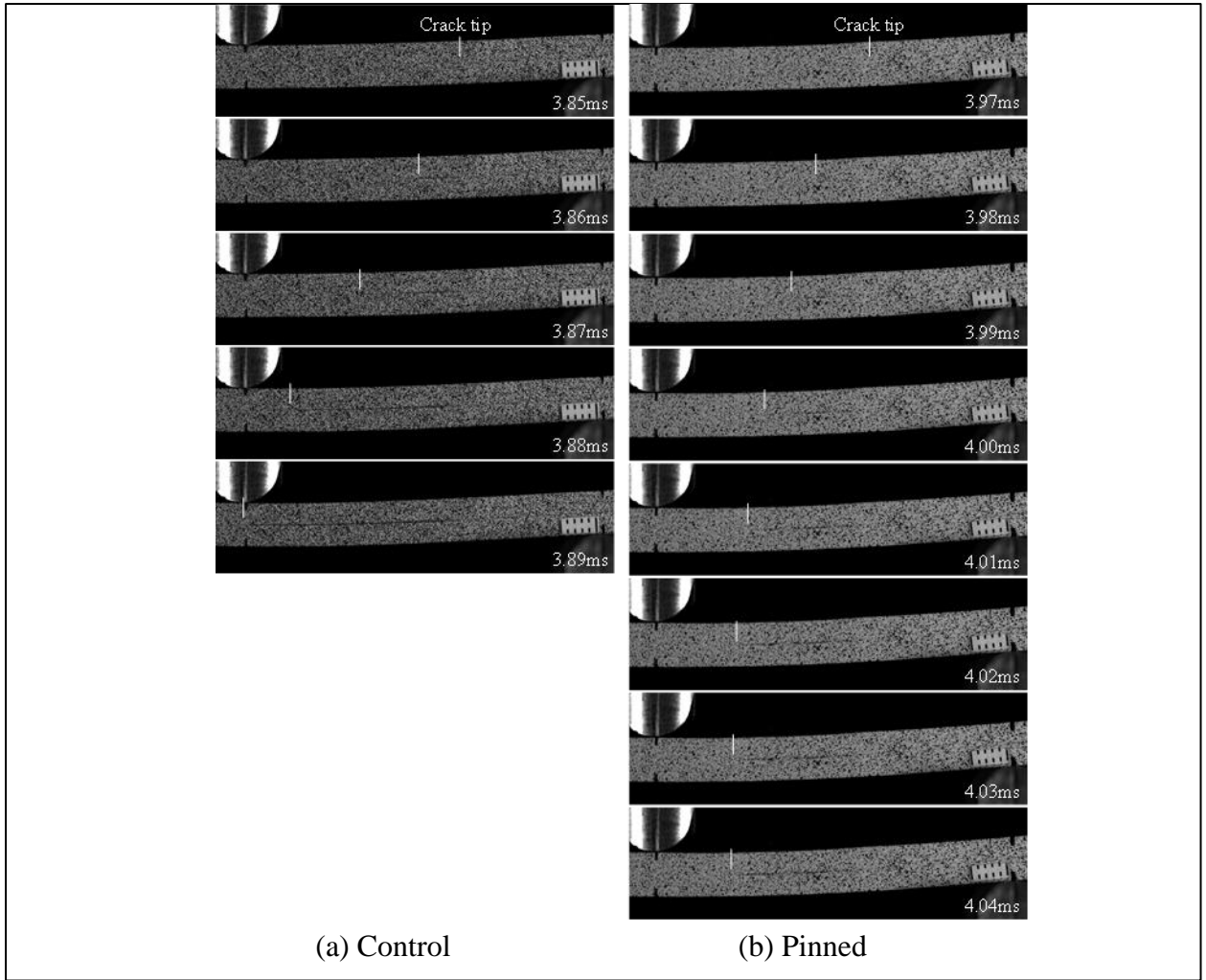
329 The delamination propagation rate (\dot{a}) was measured for each specimen directly from
330 the high speed imaging. An example of the control and pinned response to

331 delamination initiation is shown in Figure 10. For consistency, \dot{a} was calculated by
332 measuring the time taken for delamination to reach the middle loading nose ~30mm.
333 For control samples the delamination was unstable and typically propagated past the
334 middle loading nose. For the pinned samples the delmination rate varied within this
335 distance, with an almost stick slip behavior.

336 The relationship between \dot{a} and $\dot{\delta}$ is shown in Figure 11. For the control samples there
337 is a clear almost linear increase in the delamination propagation rate from 444m/s for
338 quasi-static loading rate up to 858m/s for 5.5m/s loading rate. For the pinned samples,
339 the delamination propagation rate was stable ~4mm/s when loaded quasi-statically.

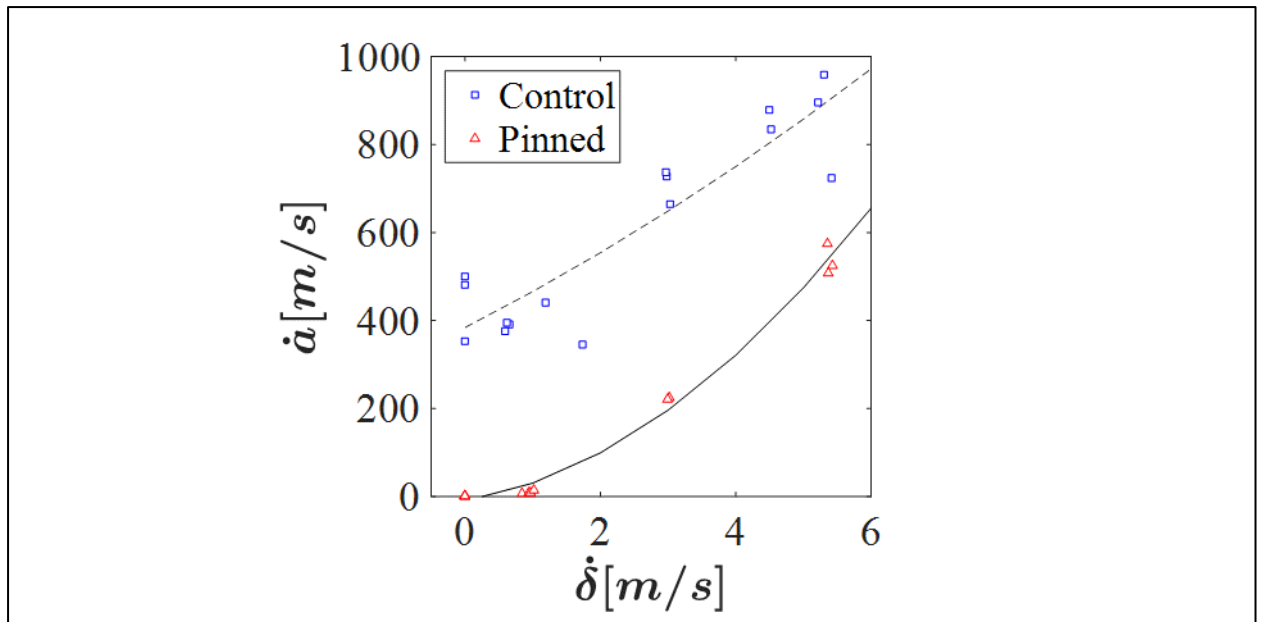
340 The propagation rate increase almost linearly from ~10m/s for 1m/s loading rate up to
341 ~530m/s for 5.5m/s loading rate.

342



343
 344
 345
 346

Figure 10 Example of the measurement of average delamination propagation rate (\dot{a}) of control and pinned samples tested with loading rate ($\dot{\delta}$) of 3m/s



347

348

Figure 11 Delamination propagation rate (\dot{a}) against loading displacement rate ($\dot{\delta}$)

349

3.3 Tensile and Shear strain rate response

350

The relationship of the shear strain rate ($\dot{\gamma}$) measured at the tip of the initial crack and

351

the tensile strain rate ($\dot{\epsilon}$) measured at the mid span length on the lower surface of the

352

specimen against displacement loading rate ($\dot{\delta}$) is shown in Figure 12. The shear

353

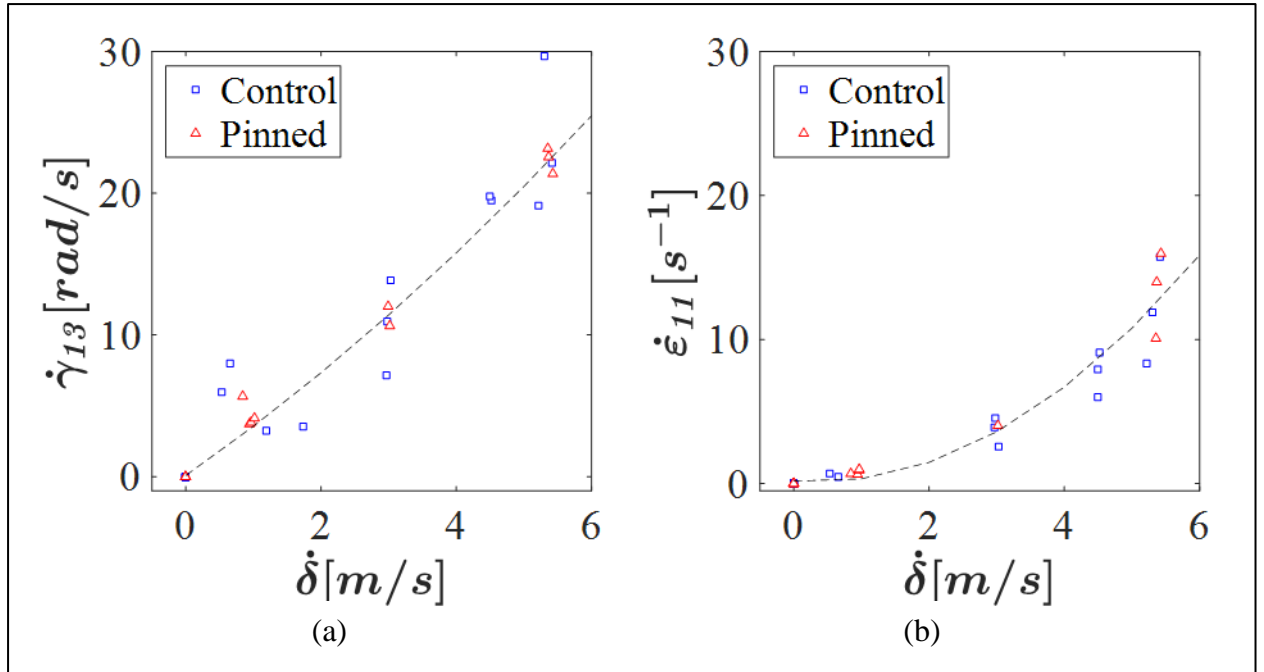
strain rate reaches an average of 22rad/s for samples tested at $\dot{\delta}$ of 5.3m/s. The

354

increase in $\dot{\gamma}$ with $\dot{\delta}$ is approximately linear. The maximum tensile strain rate

355

achieved in this investigation was on average $13s^{-1}$ for samples tested at $\dot{\delta}$ of 5.3m/s.



356

357

Figure 12 Loading displacement rate ($\dot{\delta}$) against (a) shear strain rate ($\dot{\gamma}$) and (b) tensile strain rate ($\dot{\epsilon}$)

358

3.4 Load-displacement response

359

The load-displacement plots for all the tests are given in Figure 13. With increase in

360

displacement loading rate $\dot{\delta}$ the noise in the load output measured can be seen to

361

increase and produce an unclear critical load prior to delamination. On these plots the

362

loading displacement at which delamination initiated is highlighted. It can be seen

363

that the critical load cannot be taken directly from the load displacement responses

364

necessitating the use of the compliance procedure to calculate the GIIC of the

365

specimens.

366

For the control samples, the load response appears to be constant with increasing $\dot{\delta}$.

367

For the pinned specimens, there is a significant increase in the initiation load with

368

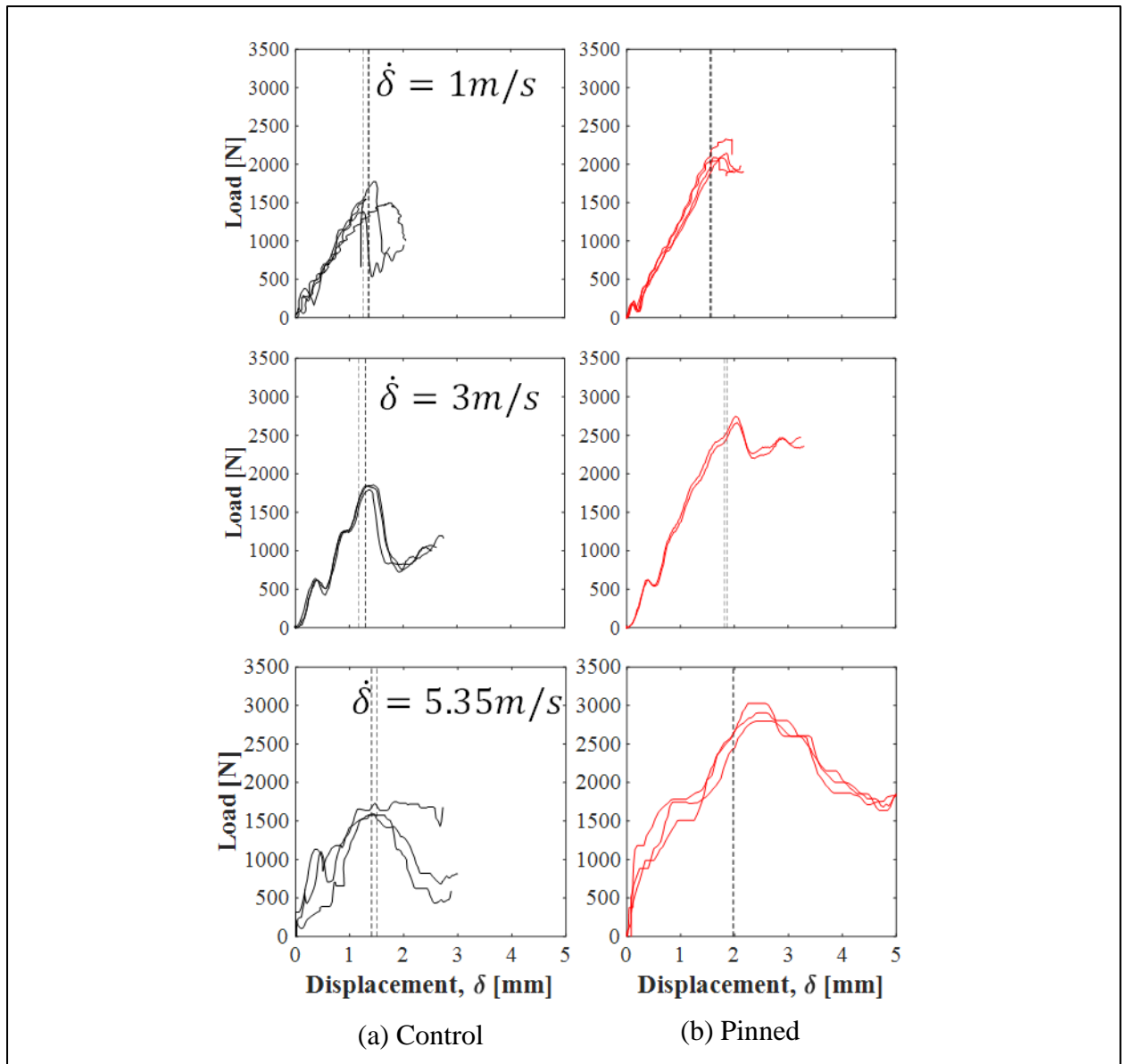
increase with $\dot{\delta}$. The pinned specimens maintain significant residual interlaminar

369

strength after delamination initiation as compared to the control samples where there

370

is a distinctly sharper load drop.



371

372 **Figure 13 Load-displacement (δ) plots of for increasing loading displacement rate ($\dot{\delta}$), dashed lines indicate**
 373 **the displacement at which delamination initiated**

374 **3.5 Rate dependence of interlaminar fracture toughness G_{IIC}**

375 The calculated G_{IIC} at the moment of delamination initiation against loading

376 displacement rate ($\dot{\delta}$), shear strain rate ($\dot{\gamma}$) and delamination velocity (\dot{a}) is presented

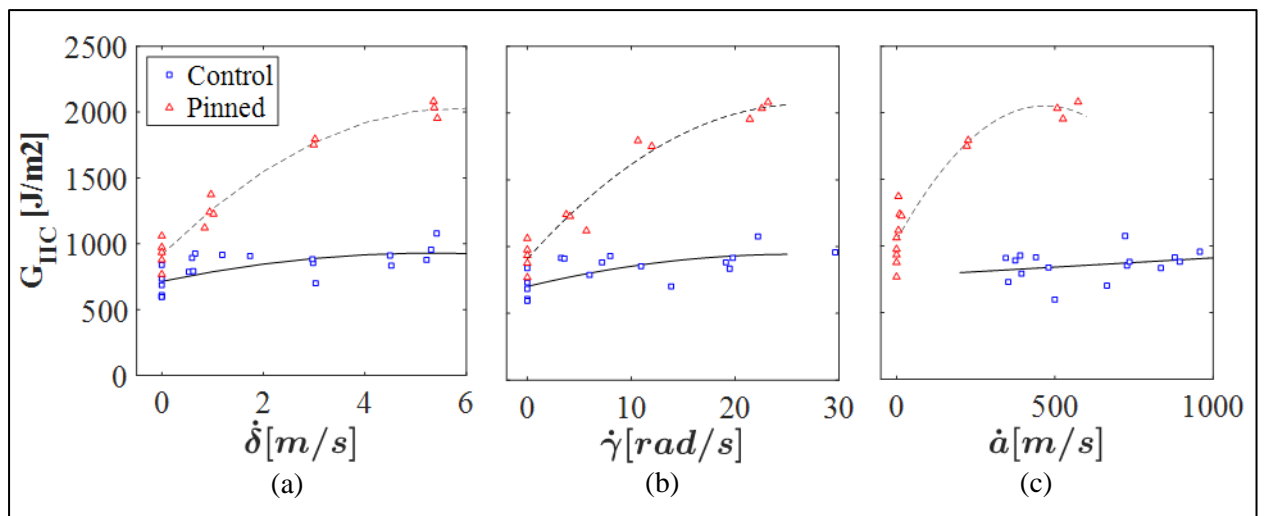
377 in Figure 14. The control samples produce a minor increase in the G_{IIC} with increase

378 in loading rate from $663 \pm 100 \text{ J/m}^2$ for quasi-static tests to $970 \pm 90 \text{ J/m}^2$ for $\dot{\delta}$ of 5.3 m/s.

379 The pinned samples showed a very strong increase in G_{IIC} with increase in loading

380 rate. With initiation G_{IIC} of $922 \pm 109 \text{ J/m}^2$ for quasi-static tests to $2002 \pm 64 \text{ J/m}^2$ for $\dot{\delta}$ of

381 5.3m/s. Since the relationship between shear strain rate and displacement rate is
 382 almost linear (Figure 12a) the response of G_{IIC} in Figure 14a and Figure 14b produce
 383 similar profile. The relationship between G_{IIC} and delamination velocity is
 384 approximately linear with very minor increase for the control samples. However, for
 385 the pinned samples, there is significant increase in G_{IIC} before what appears to be a
 386 plateau forming above 500m/s. Whether the G_{IIC} will increase with increase in
 387 delamination velocity will need to be investigated further.



388
 389 **Figure 14** G_{IIC} plots of for increasing (a) loading displacement rate ($\dot{\delta}$), (b) shear strain rate ($\dot{\gamma}$) and (c)
 390 delamination velocity (\dot{a})

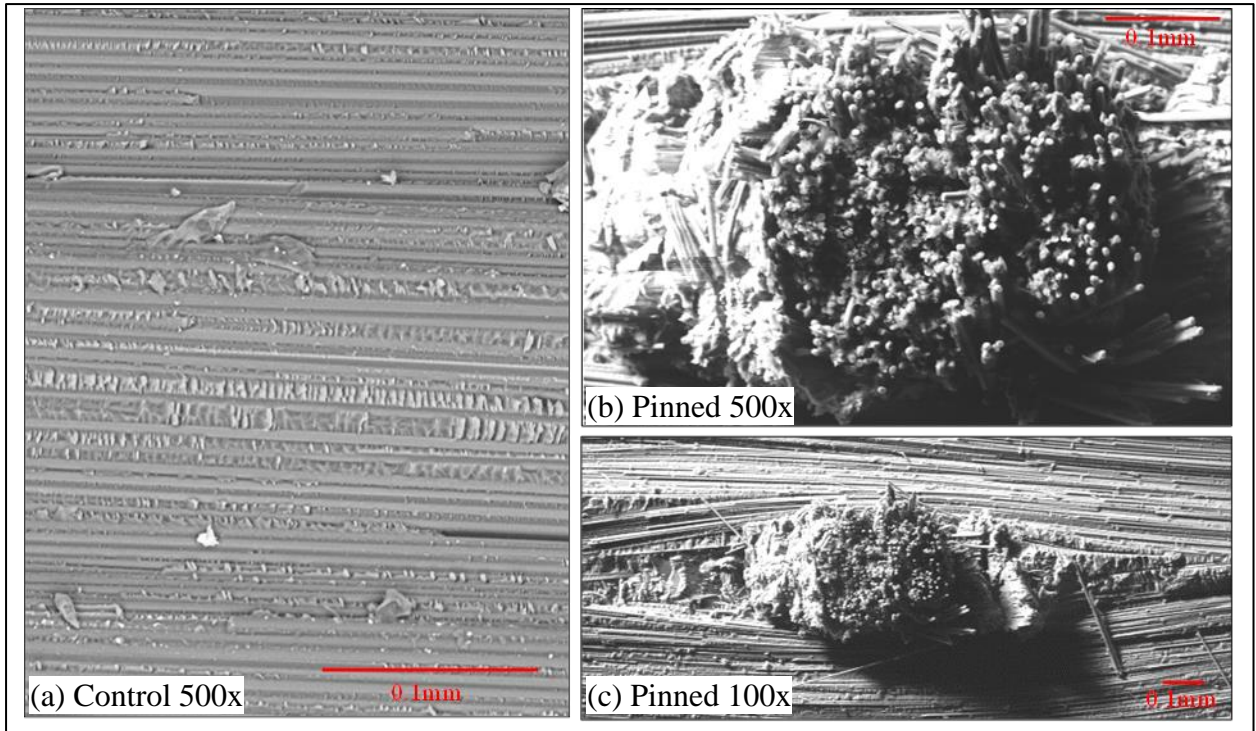
391

392 **4 Fractography**

393 A representative control and pinned specimen from each loading rate batch was
 394 manually opened and the fracture surface was observed using scanning electron
 395 microscope (SEM) imaging. It was seen that the failure profile of the pinned
 396 specimens produce two distinct morphology and this morphology was seen to
 397 transition for samples tested with loading rates above 3m/s. Figure 15 and Figure 16
 398 show the fracture surfaces of specimens loaded quasi-statically and at a loading rate $\dot{\delta}$
 399 of 5.3m/s respectively. The fracture surfaces of the control samples tested did not

400 show any significant change in surface profile, with typical shear hackles present. The
401 pinned samples tested quasi-statically showed the standard profile observed in many
402 other mode II fracture tested quasi-statically [6,39,41], in that the pins begin to pull-
403 out, bend and deform before rupture. Figure 15b and c show the small bulge of the
404 pulled-out pin that has been ruptured in a shear dominated form. Pinned specimens
405 exhibiting this failure mode will experience a long mode II bridging zone length and
406 the fracture process observed on a macro scale may be similar to a highly ductile
407 delamination crack.

408 Figure 16b and c however exhibit a flush, shear failure of the pins. This behavior is
409 reminiscence of a highly brittle fracture and has occurred in specimens tested above
410 3m/s loading rate. This behavior corresponds to a mode II delamination with a short
411 bridging zone length, since the pins do not have the time to deform, pull-out and
412 rupture. This is highlighted in the increased initiation G_{IIC} . Furthermore, the increase
413 in G_{IIC} does appear to reach an upper level plateau. This limit can be equated to an
414 experimentally and analytically predicted value of approximately 3400J/m^2 for a
415 0.28mm diameter, T700/BMI pin inserted in an array of 2% nominal areal density
416 [42–44].



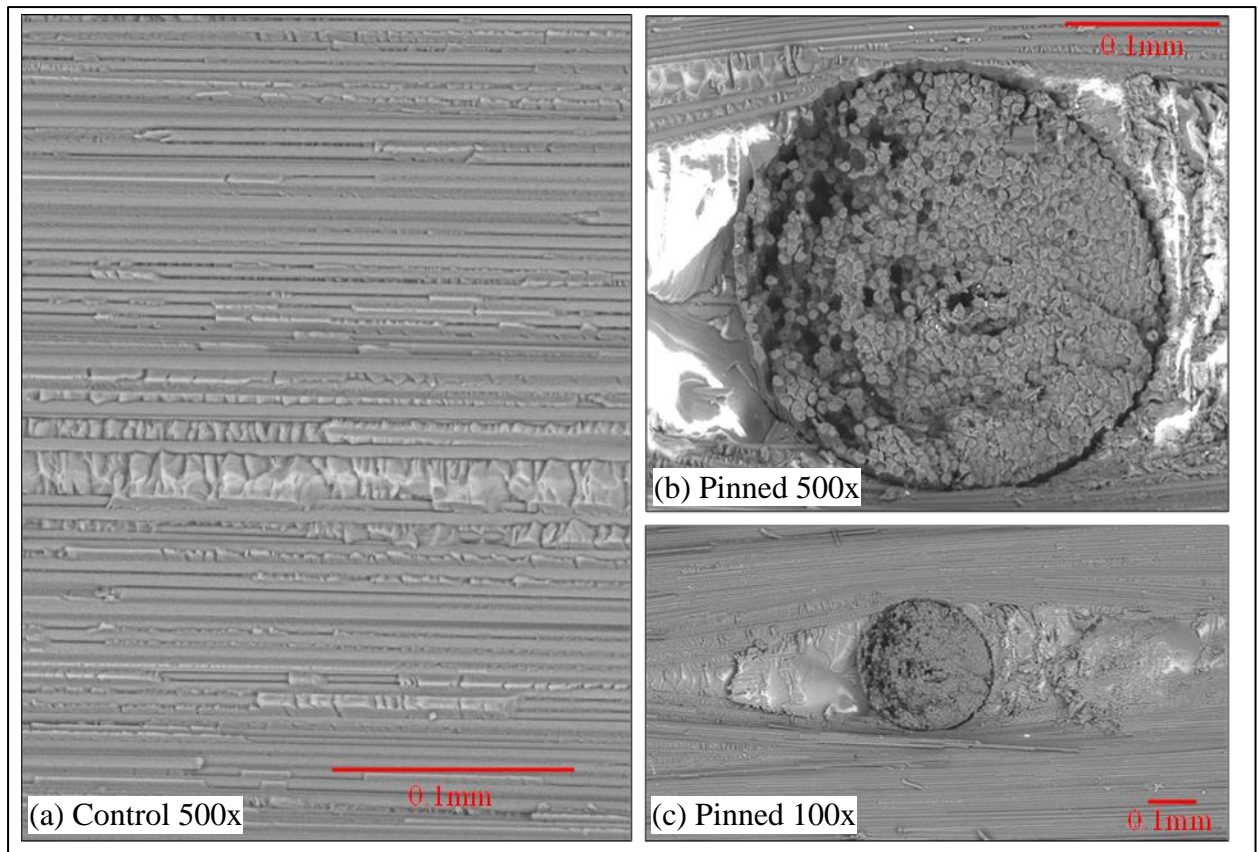
417

418

419

420

Figure 15 SEM imaging of the fracture surface of (a) control and (b,c) pinned specimens loaded quasi-statically



421

422

423

Figure 16 SEM imaging of the fracture surface of (a) control and (b,c) pinned specimens test with loading displacement rate of 5.3m/s

424

5 Discussions and Conclusions

425

A comprehensive experimental characterisation of a mode II delamination in a Z-pin

426

reinforced and unreinforced laminated composite has been carried out with increasing

427

strain rates. Tests were performed on standard hydraulic test machines for quasi-static

428

tests, instrumented drop-weight impact tower for intermediate loading rates and a

429

bespoke modified Hopkinson Bar apparatus for high loading rates. The procedure

430

followed to measure the G_{IIC} of the material used a compliance based approach rather

431

than the standard load based data reduction techniques. Assuming that the flexural

432

modulus of the beams are rate independent the G_{IIC} of each specimen was calculated

433

using the loading nose displacement at moment of delamination initiation. This

434

procedure removed the need to deduce the critical load at initiation as the load

435

response was clearly shown to be unreliable due to the excessive dynamic noise in the

436 output results. Furthermore each specimen that was tested was pre-prepared to ensure
437 a natural sharp mode II crack was created and quasi-static test showcased a good
438 agreement in G_{IIC} between the ASTM standard and the compliance method described
439 here.

440 The maximum delamination velocity achieved in the unreinforced tests was on
441 average 858m/s for 5.5m/s displacement loading rate. Falling far below the shear
442 wave speed, calculated for the current IM7/8552 composite system to be 1933m/s.
443 This highlights that higher theoretical delamination propagation rates exist and may
444 be achieved when the composite system is loaded at loading rates above 5m/s. The
445 results show that the average delamination velocity for a composite laminate will
446 increase almost linearly with increasing displacement loading rate. The range of
447 loading rates attempted in this investigation was from quasi-static to ~5.3m/s. The
448 mode II fracture toughness of the composite was seen to have a minor increase from
449 $663\pm 100\text{J/m}^2$ to $970\pm 90\text{J/m}^2$ confirming behaviours observed in literature for tests on
450 thermosetting brittle epoxy composites, where either minor or no significant increase
451 in G_{IIC} were reported.

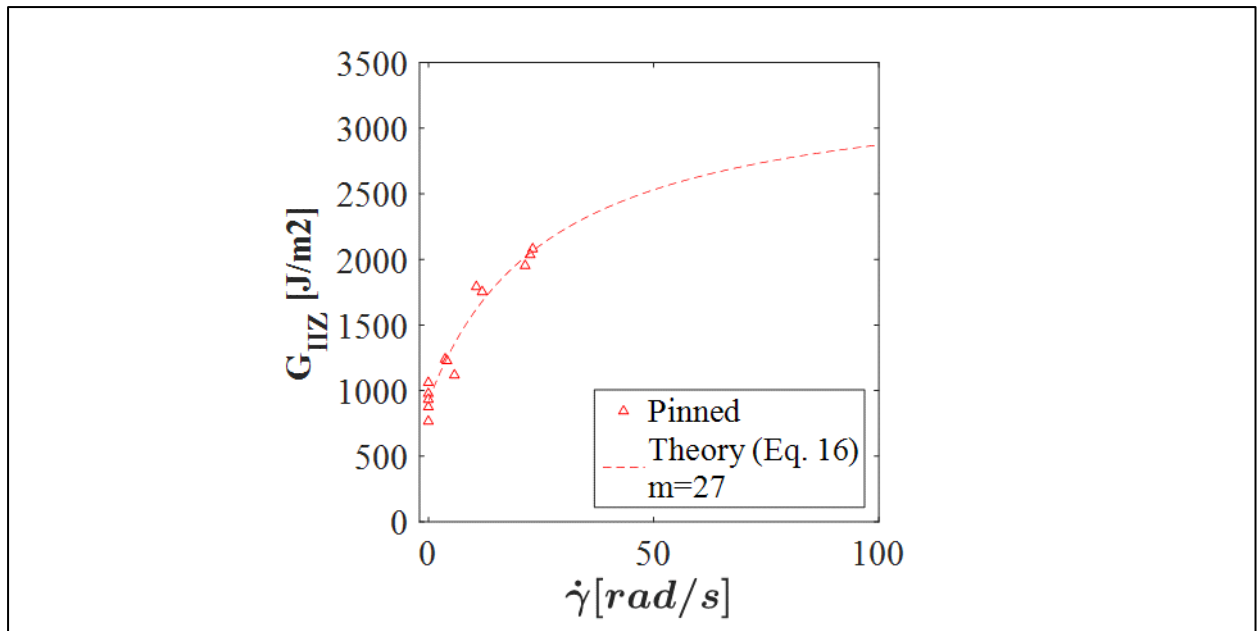
452 Mode II delamination in through-thickness reinforced laminates were also
453 characterised. These specimens exhibited a strong apparent fracture toughness
454 increase with displacement loading rate. It was shown that the initiation G_{IIC} increases
455 from 922J/m^2 to 2002J/m^2 over the velocity range tested here. Through fracture
456 surface observations a transition in the failure profile of the Z-pins was revealed. Pins
457 tested at loading rates below 3m/s corresponding to delamination velocity of
458 $\ll 200\text{m/s}$ exhibit a fracture profile similar to those tested quasi-statically, with the
459 pins pulling-out, bending before failing in shear dominated rupture. At higher than
460 3m/s loading rate the delamination velocity in the pinned samples was in excess of

461 200m/s, this resulted in a very brittle, flat fracture surface of the Z-pins. This
462 highlights that the pins did not have enough time to deform and simply failed in pure
463 shear, with a much larger contribution to the delamination traction forces and a much
464 shorter bridging zone length.

465 The results highlight how the Z-pinned composites appear to significantly improve
466 the initiation fracture toughness of a composite laminate when loaded at high strain
467 rates ($\dot{\gamma} > 10 \text{ rad/s}$). By defining G_{IIZ_min} as the apparent fracture toughness of a crack
468 with a row of Z-pins directly ahead of it (i.e. no extrinsic Z-pins bridging the crack)
469 tested at quasi-static strain rates (if G_{IIZ_min} is not available, this can be set to G_{IIC} of
470 the host material), the critical strain energy release rate of a crack behind a row of Z-
471 pins can be defined as the function of shear strain rate $\dot{\gamma}$:

$$G_{IIZ}(\dot{\gamma}) = G_{IIZ_max} \frac{G_{IIZ_min} - G_{IIZ_max}}{1 + \frac{\dot{\gamma}}{m}} \quad (16)$$

472 Where m is a fitting factor is calculated using a linear least square fit to be 27, Figure
473 17. The initiation G_{IIC} for the pinned composite does appear to asymptote towards an
474 upper limit, which can be equated to $G_{IIZ_max} \approx 3400 \text{ J/m}^2$, the theoretical maximum
475 apparent toughness for a 0.28mm diameter, T700/BMI pin inserted in an array of 2%
476 nominal areal density, calculated using single pin experiments [42–44].



477

478 **Figure 17** G_{IIz} plot against shear strain rate ($\dot{\gamma}$) showing the theoretical fit of equation (16) with $m=27$

479 The delamination response of unpinned and pinned laminates at higher displacement

480 loading rates is expected to provide the upper plateau for G_{IIC} , G_{IIz} and the

481 delamination velocity and would be important to characterize experimentally.

482 However, with increasing loading rates, the influence of kinetic energy on the

483 apparent fracture toughness calculations will become more significant and will have

484 to be fully considered. Furthermore, the delamination response to a high energy soft

485 projectile may produce significantly different failure process and thus may be an

486 interesting area to explore.

487 **6 Acknowledgements**

488 The authors would like to acknowledge Rolls-Royce plc for their support of this

489 research through the Composites University Technology Centre (UTC) at the

490 University of Bristol, UK.

491

492 7 References

- 493 [1] Kinloch AJ, Shaw SJ, Tod DA, Hunston DL. "Deformation and fracture
494 behaviour of a rubber-toughened epoxy: 1. Microstructure and fracture
495 studies," *Polymer*, vol. 24, no. 10, pp. 1341–1354, Oct. 1983.
- 496 [2] Shivakumar Gouda PS, Williams JD, Yasae M, Chatterjee V, Jawali D,
497 Rahatekar SS, Wisnom MR. "Drawdown prepreg coating method using epoxy
498 terminated butadiene nitrile rubber to improve fracture toughness of glass
499 epoxy composites," *Journal of Composite Materials*, May 2015.
- 500 [3] Yasae M, Bond IP, Trask RS, Greenhalgh ES. "Mode I interfacial toughening
501 through discontinuous interleaves for damage suppression and control,"
502 *Composites Part A: Applied Science and Manufacturing*, vol. 43, no. 1, pp.
503 198–207, Jan. 2012.
- 504 [4] Yasae M, Bond IP, Trask RS, Greenhalgh ES. "Mode II interfacial
505 toughening through discontinuous interleaves for damage suppression and
506 control," *Composites Part A: Applied Science and Manufacturing*, vol. 43, no.
507 1, pp. 121–128, Jan. 2012.
- 508 [5] Partridge IK, Yasae M, Allegri G, Lander JK. "Damage-tolerant composite
509 structures by Z-pinning," in *Toughening Mechanisms in Composite Materials*,
510 Elsevier, 2015, pp. 161–189.
- 511 [6] Yasae M, Mohamed G, Allegri G, Hallett SR. "Mixed mode delamination
512 resistance of Z-pinned multi-directional composites Part I: Experimental
513 Characterisation," *Engineering Fracture Mechanics*, 2016.
- 514 [7] Lenzi F, Riccio A, Clarke A, Creemers R. "Coupon tests on z-pinned and
515 unpinned composite samples for damage resistant applications,"
516 *Macromolecular Symposia*, vol. 247, pp. 230–237, 2007.
- 517 [8] Partridge IK, Cartie DDR. "Delamination resistant laminates by Z-Fiber
518 pinning: Part I manufacture and fracture performance," *Composites Part A:
519 Applied Science and Manufacturing*, vol. 36, no. 1, pp. 55–64, 2005.
- 520 [9] Pegorin F, Pingkarawat K, Mouritz AP. "Comparative study of the mode I and
521 mode II delamination fatigue properties of z-pinned aircraft composites,"
522 *Materials & Design*, vol. 65, pp. 139–146, Sep. 2014.
- 523 [10] Gerlach R, Siviour CR, Wiegand J, Petrinic N. "The Strain Rate Dependent
524 Material Behavior of S-GFRP Extracted from GLARE," *Mechanics of
525 Advanced Materials and Structures*, vol. 20, no. 7, pp. 505–514, Aug. 2013.
- 526 [11] Jacob GC, Starbuck JM, Fellers JF, Simunovic S, Boeman RG. "Fracture
527 toughness in random-chopped fiber-reinforced composites and their strain rate
528 dependence," *Journal of Applied Polymer Science*, vol. 100, no. 1, pp. 695–
529 701, 2006.
- 530 [12] Kusaka T, Horikawa N, Masuda M. "Low-velocity impact fracture behaviour
531 of impact-resistant polymer matrix composite laminates under mixed mode
532 loading," *Le Journal de Physique IV*, vol. 10, no. PR9, p. Pr9-317-Pr9-322,
533 Sep. 2000.
- 534 [13] You H, Yum Y-J. "Loading Rate Effect on Mode I Interlaminar Fracture of
535 Carbon/Epoxy Composite," *Journal of Reinforced Plastics and Composites*,
536 vol. 16, no. 6, pp. 537–549, Apr. 1997.

- 537 [14] Kageyama K, Kimpara I. "Delamination failures in polymer composites,"
538 *Materials Science and Engineering A*, vol. 143, no. 1–2, pp. 167–174, 1991.
- 539 [15] Blackman BRK, Dear JP, Kinloch a. J, Macgillivray H, Wang Y, Williams
540 JG, Yayla P. "The failure of fibre composites and adhesively bonded fibre
541 composites under high rates of test - Part I Mode I loading-experimental
542 studies," *Journal of Materials Science*, vol. 30, pp. 5885–5900, 1995.
- 543 [16] Compston P, Jar P-YB, Burchill PJ, Takahashi K. "The effect of matrix
544 toughness and loading rate on the mode-II interlaminar fracture toughness of
545 glass-fibre/vinyl-ester composites," *Composites Science and Technology*, vol.
546 61, no. 2, pp. 321–333, 2001.
- 547 [17] Smiley a. J, Pipes RB. "Rate sensitivity of mode II interlaminar fracture
548 toughness in graphite/epoxy and graphite/PEEK composite materials,"
549 *Composites Science and Technology*, vol. 29, pp. 1–15, 1987.
- 550 [18] Mall S, Law GE, Katouzian M. "Loading Rate Effect on Interlaminar Fracture
551 Toughness of A Thermoplastic Composite," *Journal of Composite Materials*,
552 vol. 21, no. June 1987, pp. 569–579, 1987.
- 553 [19] Maikuma H, Gillespie JW, Wilkins DJ. "Mode II Interlaminar Fracture of the
554 Center Notch Flexural Specimen under Impact Loading," *Journal of Composite
555 Materials*, vol. 24, no. 2, pp. 124–149, Feb. 1990.
- 556 [20] Major Z, Lang RW. "Rate Dependent Fracture Toughness of Plastics," in
557 *European Structural Integrity Society*, vol. 32, 2003, pp. 187–198.
- 558 [21] Barton JM. "Epoxy Resins and Composites I," in *Advances in Polymer
559 Science*, vol. 72, Berlin, Heidelberg, Berlin, Heidelberg: Springer Berlin
560 Heidelberg, 1985, pp. 111–154.
- 561 [22] Cox BN, Gao H, Gross D, Rittel D. "Modern topics and challenges in dynamic
562 fracture," *Journal of the Mechanics and Physics of Solids*, vol. 53, no. 3, pp.
563 565–596, 2005.
- 564 [23] Rosakis AJ. "Intersonic shear cracks and fault ruptures," *Advances in Physics*,
565 vol. 51, no. 4, pp. 1189–1257, 2002.
- 566 [24] Tsai JL, Guo C, Sun CT. "Dynamic delamination fracture toughness in
567 unidirectional polymeric composites," *Composites Science and Technology*,
568 vol. 61, no. 1, pp. 87–94, 2001.
- 569 [25] Colin de Verdier M, Skordos AA, Walton AC, May M. "Influence of loading
570 rate on the delamination response of untufted and tufted carbon epoxy non-
571 crimp fabric composites/Mode II," *Engineering Fracture Mechanics*, vol. 96,
572 pp. 1–10, 2012.
- 573 [26] Guo C, Sun CT. "Dynamic Mode-I crack-propagation in a carbon/epoxy
574 composite," *Composites Science and Technology*, vol. 58, no. 9, pp. 1405–
575 1410, 1998.
- 576 [27] Jiang W, Tjong S, Chu P, Li R. "Interlaminar Fracture Properties of Carbon
577 Fibre/Epoxy Matrix Composites Interleaved with Polyethylene Terephthalate
578 (PET) Films," *Polymers and Polymer Composites*, vol. 9, no. 2, pp. 141–146,
579 2001.
- 580 [28] Liu H, Yan W, Yu X, Mai Y. "Experimental study on effect of loading rate on
581 mode I delamination of z-pin reinforced laminates," *Composites Science and*

- 582 *Technology*, vol. 67, no. 7–8, pp. 1294–1301, Jun. 2007.
- 583 [29] Andrew Schlueter, Parab ND, Chen W. “Loading rate effects on mode I
584 delamination of Z-pinned composite laminates,” in *Dynamic Behavior of*
585 *Materials, Volume 1*, Cham, B. Song, D. Casem, and J. Kimberley, Eds. Cham:
586 Springer International Publishing, 2014.
- 587 [30] ASTM-D7905-14. “Standard Test Method for Determination of the Mode II
588 Interlaminar Fracture Toughness of Unidirectional Fiber-Reinforced Polymer
589 Matrix Composites,” *ASTM International*, 2014.
- 590 [31] ASTM D790-07. “Standard test methods for flexural properties of
591 unreinforced and reinforced plastics and electrical insulating materials,” *ASTM*
592 *International*, vol. (2007)e1, 2007.
- 593 [32] Hallett SR. “Three-point beam impact tests on T300/914 carbon-fibre
594 composites,” *Composites Science and Technology*, vol. 60, no. 1, pp. 115–124,
595 Jan. 2000.
- 596 [33] Gerlach R, Siviour CR, Petrinic N, Wiegand J. “Experimental characterisation
597 and constitutive modelling of RTM-6 resin under impact loading,” *Polymer*,
598 vol. 49, no. 11, pp. 2728–2737, 2008.
- 599 [34] Wiegand J, Hornig a., Gerlach R, Neale C, Petrinic N, Hufenbach W. “An
600 Experimental Method for Dynamic Delamination Analysis of Composite
601 Materials by Impact Bending,” *Mechanics of Advanced Materials and*
602 *Structures*, vol. 22, no. 5, pp. 413–421, 2015.
- 603 [35] Weeks CA, Sun CT. “Modeling non-linear rate-dependent behavior in fiber-
604 reinforced composites,” *Composites Science and Technology*, vol. 58, no. 3–4,
605 pp. 603–611, Mar. 1998.
- 606 [36] de Moura MFSF, de Morais AB. “Equivalent crack based analyses of ENF and
607 ELS tests,” *Engineering Fracture Mechanics*, vol. 75, pp. 2584–2596, 2008.
- 608 [37] Wang Y, Williams JG. “Corrections for mode II fracture toughness specimens
609 of composites materials,” *Composites Science and Technology*, vol. 43, no. 3,
610 pp. 251–256, 1992.
- 611 [38] Koerber H, Xavier J, Camanho PP. “High strain rate characterisation of
612 unidirectional carbon-epoxy IM7-8552 in transverse compression and in-plane
613 shear using digital image correlation,” *Mechanics of Materials*, vol. 42, no. 11,
614 pp. 1004–1019, 2010.
- 615 [39] Pegorin F, Pingkarawat K, Daynes S, Mouritz AP. “Mode II interlaminar
616 fatigue properties of z-pinned carbon fibre reinforced epoxy composites,”
617 *Composites Part A: Applied Science and Manufacturing*, Aug. 2014.
- 618 [40] Cartie DDR, Troulis M, Partridge IK. “Delamination of Z-pinned carbon fibre
619 reinforced laminates,” *Composites Science and Technology*, vol. 66, pp. 855–
620 861, 2006.
- 621 [41] Yasae M, Mohamed G, Hallett SR. “Multiple delamination interaction in Z-
622 pinned composites in Mode II,” *Experimental Mechanics*, 2016.
- 623 [42] Yasae M, Lander J, Allegri G, Hallett S. “Experimental characterisation of
624 mixed mode traction–displacement relationships for a single carbon composite
625 Z-pin,” *Composites Science and Technology*, vol. 94, pp. 123–131, 2014.
- 626 [43] Allegri G, Yasae M, Partridge IK, Hallett SR. “A novel model of

- 627 delamination bridging via Z-pins in composite laminates,” *International*
628 *Journal of Solids and Structures*, vol. 51, no. 19–20, pp. 3314–3332, Oct. 2014.
- 629 [44] Zhang B, Yasaei M, Hallett SR, Allegri G. “Micro-Mechanical Finite Element
630 Analysis of Z-pins under Mixed-Mode Loading,” *Composites Part A: Applied*
631 *Science and Manufacturing*, 2015.
- 632